American Mineralogist, Volume 97, pages 883–889, 2012

Investigation of cation ordering in triclinic sodium birnessite via ^{23}Na MAS NMR spectroscopy

Kellie A. Aldi,[1] Jordi Cabana,[1,*] Paul J. Sideris,[1,†] and Clare P. Grey[1,2,‡]

[1]Department of Chemistry, Stony Brook University, Stony Brook, New York 11794, U.S.A.
[2]Department of Chemistry, University of Cambridge, Lensfield Road, Cambridge CB2 1EW, U.K.

Abstract

Birnessite is a widespread, naturally occurring layered manganese oxide that exerts significant influence over the geochemical cycling of environmentally relevant cations due to its high-interlayer adsorption capacity. Triclinic sodium birnessite was used as a synthetic analog to gain a better understanding of the nature of cation adsorption in this important phyllomanganate. Drawing from previous work correlating observed ^{23}Na NMR shifts in manganese oxides with local environment and Mn oxidation state, the ^{23}Na NMR spectra of metastable buserite and two birnessite samples, NaBi-H-I and NaBi-II, were analyzed to determine the nature of the bound interlayer sodium ions in these materials. The small ^{23}Na chemical shift of buserite shows that its interlayer sodium is fully hydrated. X-ray diffraction indicates that NaBi-H-I is a disordered birnessite while NaBi-II is highly crystalline. High-field (14.1 T) fast MAS NMR spectra of NaBi-H-I and NaBi-II supports these observations, resolving multiple sodium environments for NaBi-H-I and only two sodium environments for NaBi-II. The observed hyperfine shifts were less than expected for sodium environments with manganate layers composed of 2/3 Mn^{4+} and 1/3 Mn^{3+} ions, and the ^{23}Na line shapes indicated that the Na^+ ions are in distorted environments. Both these factors suggest that the sodium ions are offset in the interlayers toward a single oxide layer and located near Mn^{3+}-rich environments within the layer.

Keywords: Manganese oxides, birnessite, NMR, paramagnetic

Introduction

Manganese oxides are ubiquitous in the environment, particularly at the interface between the lithosphere and the hydrosphere (Post 1999). They commonly occur as thin grain coatings on several minerals, or as crusts of deep-sea nodules that cover large expanses of ocean and lake bottoms. Many studies have investigated the important role of manganese oxides in the sequestration of metals (Lanson et al. 2002b; Mckenzie 1967, 1980; O'Reilly and Hochella 2003; Pena et al. 2010; Sherman and Peacock 2010).

Numerous studies of microbial production of layered manganese oxides suggest that these biogenically produced materials play a crucial role for environmental remediation (i.e., the sequestration of toxins in the environment) (Bargar et al. 2009; Fuller and Harvey 2000; Harvey and Fuller 1998; Toner et al. 2006). Due to their prevalence in the environment and their high-adsorption capacities, these minerals are an important control of heavy metals and other trace elements in soils and aquatic sediments (Post 1999).

Studies have indicated that phyllomanganates, i.e., layered Mn oxides, are the dominant type of manganese oxide in the environment (Bargar et al. 2009; Glasby 1977; Villalobos et al. 2006, 2003) and that birnessite is the most common form of naturally occurring layered manganese oxides (Post 1999). Birnessite is composed of stacked sheets of edge-sharing manganese (IV) octahedra containing a negative layer charge arising from the presence of layer vacancies and/or manganese (III) octahedra. To offset this negative layer charge, cations, and protons are sorbed within the interlayers (Fig. 1a). Birnessite was determined to have one of the highest sorptive capacities for heavy metal cations that are of environmental interest (O'Reilly and Hochella 2003).

The typical interlayer spacing of manganese oxide layers in birnessite is about 7 Å, but this varies according to the nature of the cations present in the interlayer space (Golden et al. 1986; Johnson and Post 2006; Lopano et al. 2007). Natural samples of birnessite generally occur as poorly crystallized and fine-grained particles, resulting in very broad reflections in the corresponding X-ray diffraction powder patterns that complicate their structural characterization (Glasby 1977; Post 1999). Previous work has confirmed that synthetic birnessite is a good structural representative of naturally occurring birnessites and it can be prepared in more crystalline forms (i.e., larger particle sizes and greater ordering of layer stacking), rendering it easier to characterize (Glasby 1977; Kuma et al. 1994). Synthetic birnessite prepared by high-pH precipitation methods are reported to contain vacancy-free manganate layers, rich in Mn^{3+}. Birnessite forms initially as a hydrated metastable intermediate phase commonly referred to as buserite (Feng et al. 2000) containing extra interlayer waters propping the manganate layers apart at an interlayer spacing of 10 Å. By acidifying a suspension of metastable buserite, one can also form a hexagonal birnessite, for which the layer charge now arises predominantly from layer manganese vacancies that result

* Present address: Environmental Energy Technologies Division, Lawrence Berkeley National Laboratory, 1 Cyclotron Road MS62R0203, Berkeley, California 94720, U.S.A.
† Present address: Department of Astronomy and Physics, Hunter College of CUNY, 695 Park Avenue, New York, New York 10065, U.S.A.
‡ E-mail: cpg27@cam.ac.uk

0003-004X/12/0506–883$05.00/DOI: http://dx.doi.org/10.2138/am.2012.3933

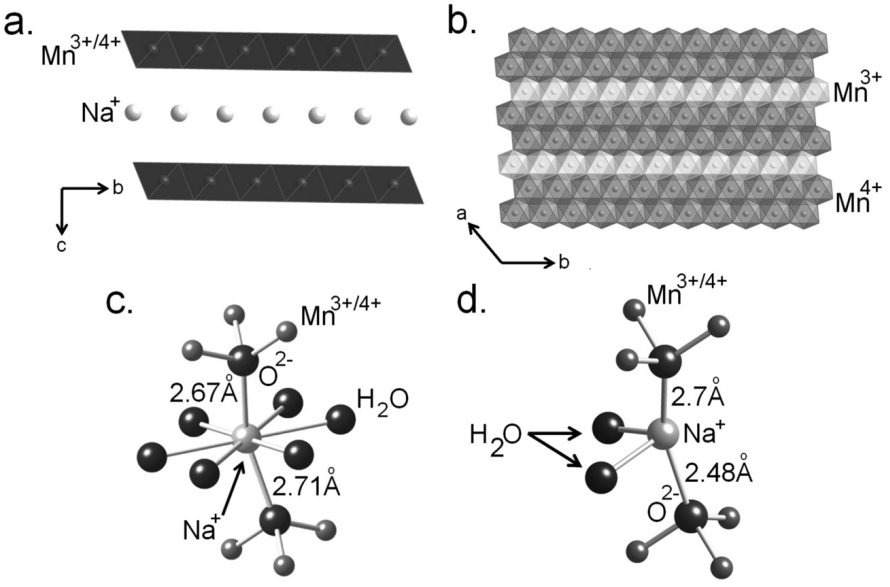

FIGURE 1. (**a**) Idealized structure of the phyllomanganate, birnessite, composed of layers of manganese octahedra, sandwiching interlayer cations. Interlayer species may consist of water and various cations to offset the negative layer charge. (**b**) Suggested ordering of Mn^{3+} ions within the manganese oxide layers (Lanson et al. 2000). Mn^{3+} ions (light gray octahedra) order in rows along the **b** axis separated by two rows of Mn^{4+} ions (dark gray octahedra). (**c**) Local sodium environment as proposed by Post et al. (2002). Sodium is coordinated to six interlayer waters at distances of 2.85 to 2.95 Å and two layer O atoms at 2.71 and 2.67 Å. There are six Na^{+}-O-$Mn^{3+/4+}$ interactions resulting from coordination to two layer O atoms above and below the sodium site. (**d**) Local sodium environment as proposed by Lanson et al. (2002a). Sodium is coordinated to two layer O atoms at 2.48 and 2.74 Å and two interlayer water molecules at 2.61 and 2.74 Å.

from the dissolution of Mn^{2+} caused by the ready disproportionation of layer Mn^{3+} (Lanson et al. 2000).

There have been numerous studies investigating the structure of synthetic birnessite, however differences in synthetic methods and considerable disorder and structural variability of this layered material have led to some ambiguities. For example, depending on the synthetic method and the interlayer cation species present, layer stacking may vary, as well as the amounts, coordination geometry, and distribution of interlayer species, along with the layer charge and vacancy concentration (Drits et al. 1997; Lanson et al. 2000). The high-sorptive capacities are linked to the structural features of the layers. Many studies have probed the nature of the cation ordering and how this correlates with layer Mn vacancy and Mn^{3+} concentrations, primarily through techniques that give information on long-range ordering of interlayer cations such as Rietveld refinement of X-ray diffraction, and selected-area electron diffraction (SAED) data (Drits et al. 1997; Kuma et al. 1994; Post and Veblen 1990). Characterizations of the short range local environment of hexagonal, triclinic, and cation exchanged birnessites have also been performed via EXAFS and provide valuable structural insights (Manceau et al. 2002; Silvester et al. 1997; Webb et al. 2005), but definitive assignments of possible interlayer cation ordering, particularly with respect to the manganese oxide layer, have yet to be obtained.

In the case of the triclinic high-pH form of synthetic sodium birnessite, the heterovalent manganese ions are proposed to order into Mn^{3+}-rows parallel to the **b** axis, separated by two Mn^{4+}-rich rows (Fig. 1b) (Drits et al. 1997; Kuma et al. 1994). This ordering is used to explain the observed lengthening of the *a* lattice parameter, an elongation in this direction is minimizing steric strains from an azimuthally oriented Jahn-Teller axial elongation of Mn^{3+}-O bonds (Gaillot et al. 2007; Lanson et al. 2002a). Jahn-Teller distortions are typically observed in compounds containing >20–30% of the Jahn-Teller ion, Mn^{3+}, in the structure (Rogers et al. 1965). The ordering of interlayer species is generally less agreed upon; several studies are diverging on the issue of the positioning of interlayer sodium cations. Rietveld refinements and difference electron Fourier mapping by Post et al. (2002) and Lopano et al. (2007) produced a model with interlayer sodium cations placed nearly centered between the layers on a split Na/H_2O site, coordinated by six interlayer waters and two layer O atoms above and below the sodium (Fig. 1c) (Lopano et al. 2007; Post et al. 2002), resulting in two long $Na\text{-}O_{layer}$ bond distances of 2.6–2.7 Å. In contrast, forward simulations of the sodium birnessite X-ray diffraction powder pattern by Lanson et al. (2002a) produced a model in which interlayer sodium is placed on a split site that is coordinated to two interlayer waters and two layer oxygen atoms, one above and one below (Fig. 1d). This split site is shifted along the **c** axis, generating $Na\text{-}O_{layer}$ bond distances of 2.46 and 2.74 Å. Unfortunately nuances in the placement of interlayer cations in sodium birnessite were difficult to isolate via refinements/simulations of X-ray diffraction patterns or difference electron Fourier mapping due to positional disorder of interlayer species. Gaining insight into the local coordination environment of interlayer cations in the birnessite structure will enrich the understanding of the cation exchange and sorption properties associated with this phyllomanganate.

^{23}Na magic angle spinning nuclear magnetic resonance (MAS NMR) spectroscopy has been successfully used to investigate several paramagnetic materials (Carlier et al. 2009) and is applied here to the study of the local environments in Na-birnessite since the method is sensitive to coordination number, geometry, and short-range ordering, as well as oxidation state. ^{23}Na is an I = 3/2 nucleus with a moderately sized quadrupolar moment (0.14×10^{-28} m^2 A), and hence, second-order quadrupolar line shapes are observed under MAS at moderate fields, complicating the interpretation of the NMR spectrum. Although the use of higher magnetic fields reduces the second-order effects, it also increases the size of

the dipolar interactions between the paramagnetic ions, Mn^{3+} and Mn^{4+}, and the sodium ions (in frequency units), necessitating the use of fast MAS (Grey and Dupré 2004).

The presence of a paramagnetic ion introduces yet another strong interaction in the ^{23}Na spectra, but one that contains information concerning the local crystallographic and electronic structure. The unpaired spin density of a paramagnet may be transferred through the bonds with an anion, producing a Fermi contact interaction that results in a significantly larger shift of the isotropic resonances of the observed nucleus than those typical of diamagnetic systems, particularly for lighter elements (Gray and Dupre 2004). Based on experimental studies, these interactions are generally believed to be additive (Cheetham et al. 1987), the overall Fermi-contact shift being the result of the individual contributions of each existing M-X-A (M = paramagnet, X = anion, A = observed nucleus) contact. However, the magnitude of this contribution will be strongly dependent on bond angles, distances, and the oxidation state of the contributing paramagnet (Gray and Dupre 2004). In practice, such values have been obtained through the analysis of model compounds with known structures, although theoretical studies of the shifts are starting to contribute to this process (Carlier et al. 2003).

Previous work has investigated the hyperfine shift contributions of Mn^{3+} and Mn^{4+} to observed ^{23}Na NMR spectra of various sodium manganese oxides, including the Mn^{3+} materials α- and β-$NaMnO_2$, and the mixed Mn^{3+}/Mn^{4+} materials (Aldi et al. in preparation). The contribution to the overall shift was analyzed and larger contributions were observed for Mn^{4+}-O-Na contacts than Mn^{3+}-O-Na contacts. However, the magnitudes of these interactions were found to be strongly dependent on bonding angles, bond lengths, and the presence of Jahn-Teller distortion. These trends are used to help rationalize the ^{23}Na NMR spectra of the synthetic sodium buserite and birnessite samples investigated in this study.

This current work provides insight into structural the spatial ordering of sodium cations within the interlayer space of buserite and birnessite, as well as the arrangement of interlayer cations with respect to Mn^{3+} and Mn^{4+} ions within the layer. We use ^{23}Na MAS NMR at multiple fields to obtain resolution of the sodium environments present in birnessite samples prepared by different synthetic methods. The magnitudes of the shifts observed in the NMR spectra are used to explain cation positions relative to the manganate layers.

Experimental methods

Synthesis

Two different synthetic routes available in the literature that produce birnessite samples with different structural features were chosen for this study. The first synthetic method was taken from optimized parameters reported by Feng et al. (2000, 1997): a 0.6 *M* solution of freshly prepared NaOH in 3% H_2O_2 was slowly added to a 0.3 *M* solution of $Mn(NO_3)_2$ with vigorous stirring, immediately forming a dark black/brown precipitate. The reaction was stirred for 5 min after the complete addition of NaOH/H_2O_2 solution and then aged overnight without stirring. The final precipitate was filtered, washed with copious amounts of de-ionized water and air-dried. A small amount of sample was retained at this point and is denoted: NaBi-I. Once dried, the powder was then re-suspended in a 2 *M* solution of NaOH in a polytetrafluoroethylene-lined stainless steel hydrothermal vessel and hydrothermally treated at 175 °C for 24 h. Finally, the sample was filtered, washed with deionized water and air-dried. The product of the hydrothermally treated material from this synthetic method is denoted: NaBi-H-I.

In the second synthetic method, first reported by Giovanoli et al. (1970), a 0.5 *M* solution of $Mn(NO_3)_2$ was aerated with O_2 gas through a glass frit at a rate of ~2 L/min under vigorous stirring for ~20 min, after which a 5.5 *M* solution of NaOH was added. Afterward, the reaction was run under O_2 gas aeration and stirred for 5 h. Finally, the black/brown precipitate was filtered and washed with copious amounts of deionized water until the pH of the effluent was ~8. A small amount of the isolated material was kept as a wet paste and is denoted NaBu-II. The rest of the material was air-dried and is denoted NaBi-II.

Powder X-ray diffraction (XRD)

Powder X-ray diffraction data was collected on a Scintag diffractometer (Cu*K*α radiation, λ = 1.54 Å) or a Rigaku Miniflex diffractometer (Cr*K*α radiation, λ = 2.29 Å). A step scan of 0.2°, 2θ, was used for all data collection with a scan speed of 1°/min. All data were collected with or converted to Cu*K*α radition for clarity. Diffraction patterns were matched to the JCPDS pattern cards in the diffraction pattern library.

Magic angle spinning (MAS) NMR

^{23}Na MAS NMR experiments were performed at 52.8 MHz on a CMX-200 spectrometer in a field of 4.7 T using a 1.8 mm MAS probe at rotor spinning speeds (ν_r) of 38–40 kHz. Additional experiments were performed at 95 and 158.4 MHz using fields of 8.4 and 14.1 T, respectively, using a 1.3 mm MAS probe, with spinning speeds of 58–60 kHz. Both probes were designed and built by A. Samoson and co-workers (NICFB, Tallinn, Estonia). A rotor synchronized spin-echo pulse sequence (90°-τ-180°-τ_1-acquisition) was used with typical 90° and 180° pulses of 1.3 and 2.6 μs, respectively. Evolution periods were $\tau = n/\nu_r$, where n = 2, 3, and $\tau_1 = \tau - 20$ μs. A 1 *M* solution of ^{23}NaCl was used as a reference at 0 ppm.

NMR simulations

^{23}Na NMR spectra were modeled using the program WinSolids1 by K. Eichele. Values for quadrupolar coupling constant (χ), the asymmetry parameter (η), and the isotropic shift (δ_{iso}) were refined. Line broadening was also varied between Gaussian and Lorentzian to achieve the best fit.

Results

XRD

X-ray diffraction was used to investigate the effect of the synthetic method on the birnessite structure and crystallinity.

The synthesis of NaBi-H-I includes a hydrothermal step

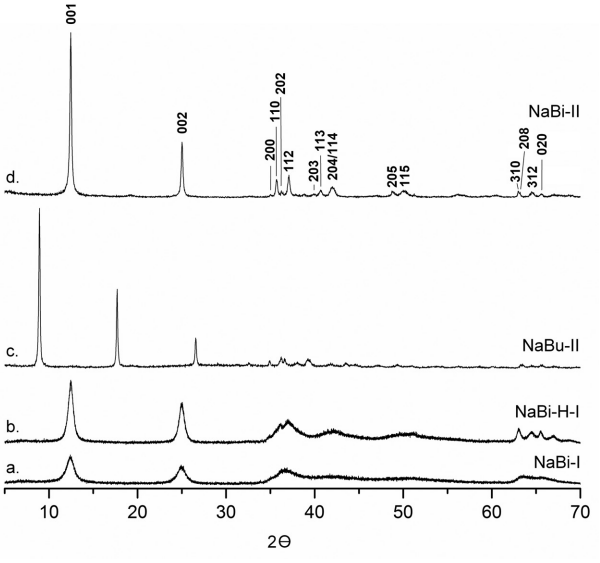

Figure 2. XRD patterns of triclinic birnessite synthesized via different synthetic methods. (**a**) NaBi-I (before hydrothermal treatment), (**b**) NaBi-H-I (after hydrothermal treatment), (**c**) NaBu-II, the metastable buserite phase formed during the synthesis of NaBi-II, and (**d**) NaBi-II.

whereby the particle size of the material is increased (Feng et al. 1997, 2000; Liu et al. 2000). Comparison of the XRD powder patterns of the NaBi-H-I material before and after hydrothermal treatment shows a narrowing of the Bragg reflections, as well as an increase in reflection intensity (Figs. 2a–2b). Nonetheless, even the post-hydrothermal treatment sample still exhibits fairly broad Bragg reflections with weak intensities, including broadened 20*l* and 11*l* peaks around 2θ = 35° and split 31*l* and 02*l* peaks around 2θ = 64°, consistent with turbostratically stacked triclinc birnessite (Drits et al. 2007). Conversely, the NaBi-II sample, prepared via oxidation of Mn^{2+} in solution by aerating the solution with O_2 gas, produces a more crystalline triclinic birnessite (Fig. 2d) typically associated with more ordered layer stacking (Drits et al. 2007; Lanson et al. 2002a). The NaBu-II sample, isolated before the drying process of the synthesis of NaBi-II, also exhibits high crystallinity but with a larger interlayer spacing (~10 Å), consistent with the extra interlayer waters present in the metastable buserite phase (Fig. 2c) (Johnson and Post 2006).

NMR

^{23}Na MAS NMR spectra were acquired both for the hydrated buserite phase, NaBu-II (material was run as a wet paste) and for the subsequently dried birnessite phase, NaBi-II (Fig. 3). The difference in the local environment of sodium in both phases is apparent from the two spectra. The NaBu-II (Fig. 3a) shows a narrow resonance at 19 ppm, the small shift being consistent with sodium ions in a diamagnetic environment (Mackenzie and Smith 2002). The total absence of peaks with large shifts strongly suggests that these Na^+ ions are fully hydrated within the buserite framework preventing direct interaction with the paramagnetic [MnO_2] layers. This would also imply that hydrogen bonding between interlayer water and the manganese oxide layers is the dominant interaction that holds the layers together. Once the material is dried to the birnessite form (Fig. 3b) a broad and complex lineshape with discontinuities at 270 and 347 ppm is observed. The shifts clearly indicate that the Na-O_{layer} distances are now short enough for the spin density from the $Mn^{3+/4+}$ ions to be transferred to the Na^+ ion. This is in contrast with reports from Potter and Rossman (1979) that IR spectra indicate interlayer cations, which are only weakly bound to the manganate layers in birnessite.

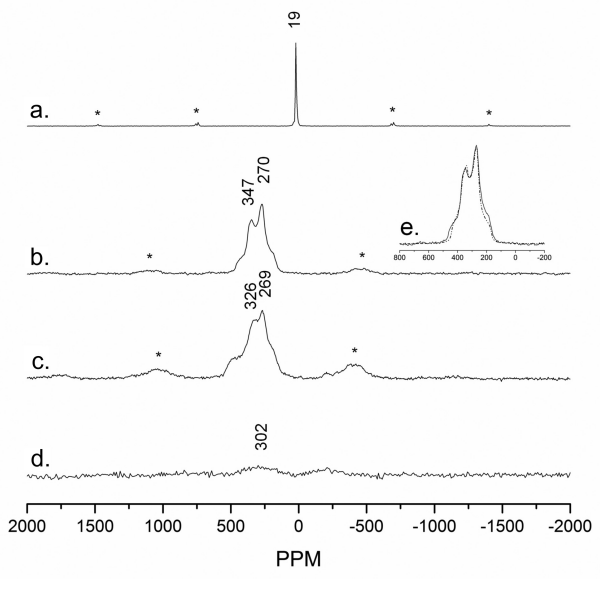

FIGURE 3. ^{23}Na MAS NMR spectra of (**a**) NaBu-II. (**b**) NaBi-II. (**c**) NaBi-H-I. (**d**) NaBi-H-I. All spectra were acquired in a 4.7 T field at spinning speeds of 35–40 kHz. Spinning sidebands are marked with an asterisk. (**e**) Inset of spectrum **b** is a simulation of the central transition of NaBi-II, where values for χ, η, δ_{iso} were extracted for two sites. Site 1: $\chi = 2.9 \pm 0.05$ MHz, $\eta = 0.69 \pm 0.03$, $\delta_{iso} = 444 \pm 4$ ppm; Site 2: $\chi = 2.8 \pm 0.025$ MHz, $\eta = 1.0 \pm 0.05$, $\delta_{iso} = 370 \pm 2$ ppm. The relative intensity of Site 1 to Site 2 used in the simulation is 0.6:1.

Solid-state ^{23}Na NMR is sensitive to slight variations in local environment, which can be manifested in distributions of chemical shifts and quadrupolar interactions, both giving rise to broadened resonances. Comparison of the ^{23}Na NMR spectra of the Na-birnessite materials NaBi-I, NaBi-H-I, and NaBi-II indicates that the crystallinity is correlated with the definition, or lack thereof, of the spectral lineshape (Figs. 3b–3d). The NaBi-I material shows the most featureless NMR spectrum (Fig. 3d), whereas some distinct peaks clearly become noticeable after hydrothermal treatment (Fig. 3c). Liu et al. (2000) observed that both particle size and sodium content appear to increase upon hydrothermal treatment of the initial disordered birnessite phase, consistent with the weaker signal for NaBi-I compared to NaBi-H-I. The lack of resolution in the NaBi-I material may be due to a disordered arrangement of Mn^{4+} and Mn^{3+} within the manganese oxide layers, or turbostratic layer stacking. Likewise, the increase in defined spectral features observed from pre- to post-hydrothermal treatment is likely due to an increase in Mn^{3+} and/or layer stacking order within the framework of the birnessite structure after hydrothermal treatment. In contrast to both the pre- and post-hydrothermally treated NaBi-I material, the ^{23}Na MAS NMR spectrum of the crystalline NaBi-II material (Fig. 3b) has the most well-defined discontinuities of the three spectra, which is linked to the existence of the highest degree of ordering of Mn^{3+} within the birnessite layers and/or the highest degree of sodium ordering of all the samples.

The high-field (8.4 and 14.1 T) ^{23}Na NMR spectra of the NaBi-II and NaBi-H-I materials (Figs. 4a–4d) provide more conclusive information about layer charge distribution and sodium ordering within the interlayers as greater resolution of local environments is achieved for the second-order quadrupolar broadened lineshapes. Note that an increase in magnetic fields necessitate the use of faster spinning speeds (59–60 kHz) to avoid isotropic resonance-sideband overlap. The decrease in peak width and the increase in peak resolution confirm that the complex lineshapes observed at 4.7 T arise from large quadrupolar interactions for both the NaBi-H-I and NaBi-II material. The broad isotropic resonances observed in the 4.7 T spectrum of NaBi-II are resolved into two distinct sodium sites at 334 and 408 ppm at a field strength of 14.1 T (Fig. 4d). The simplicity of the spectra suggests a highly ordered, relatively simple distribution of sodium with respect to the manganese oxide layers. The intensities of the peaks in these spectra are quantitative and can be used to obtain a relative ratio between the two sites of nearly

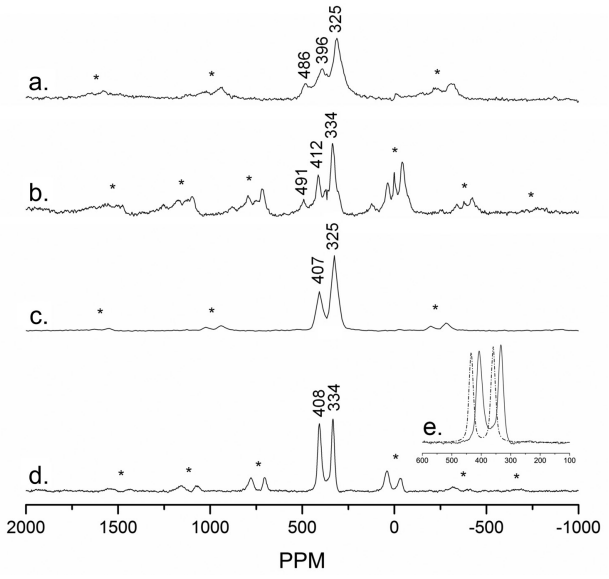

FIGURE 4. (**a**) ^{23}Na NMR spectra of NaBi-H-I at a 8.4 T field strength and (**b**) at 14.1 T with spinning speed of 60 kHz. (**c**) ^{23}Na NMR spectra of NaBi-II at a 8.4 T field strength and (**d**) at 14.1 T with spinning speeds of 59 kHz. Spinning sidebands are marked with an asterisk. (**e**) Spectral simulation of the central transition in **d** using the χ, η, δ_{iso} values refined for two sites in the 4.7 T spectrum. See Figure 3e. Site 1: $\chi = 2.9 \pm 0.05$ MHz, $\eta = 0.69 \pm 0.03$, $\delta_{iso} = 444 \pm 4$ ppm; Site 2: $\chi = 2.8 \pm 0.025$ MHz, $\eta = 1.0 \pm 0.05$, $\delta_{iso} = 370 \pm 2$ ppm. Spectral simulation used a relative intensity of 0.93:1 for sites 1:2 at 14.1 T field strength.

1:1 when spinning sideband intensity is included.

The central transition of NaBi-I spectra at 4.7 and 14.1 T field strengths were simulated by using two sodium sites, referred to as Sites 1 and 2 (see insets, Figs. 3e and 4e). Relative to the intensity of Site 2, the intensity of Site 1, obtained from the simulation of the 4.7 T spectrum, was 60%, whereas it was 93% in the 14.1 T spectrum. The reasons for this are not entirely clear, but may be due to a combination of the slightly larger quadrupolar coupling constant of Site 1, coupled with differences in the dipolar coupling, resulting in more central transition intensity contained within the spinning sidebands for the Site 1 resonance at lower fields. The peaks of the 14.1 T simulation are shifted relative to the lower field spectrum, which is attributed to the temperature sensitivity of the ^{23}Na hyperfine shifts. The drive and bearing air used for MAS generates frictional heat, raising sample temperatures relative to the ambient room temperature. Higher sample temperatures have been noted to produce smaller hyperfine shifts in the NMR spectra other paramagnetic materials (Kim et al. 2010). This effect was not taken into account in the spectral simulation. The parameters obtained in these simulations gave large values for the asymmetry parameter, η, for both environments: $\eta = 0.7$ for Site 1, and $\eta = 1.0$ for Site 2.

The NaBi-H-I material gives a similar spectrum at 4.7 T to that of the NaBi-II material (Fig. 3c) but with slightly less well-defined discontinuities at 269 and 326 ppm and shoulders at 188 and 495 ppm. As the field strength increases, the resolution of several sodium sites is achieved. At 14.1 T, clear isotropic resonances at 334, 412, and 491 ppm emerge, with a slight shoulder at 300 ppm that could be an additional sodium site (Fig. 4b). Of particular significance is the fact that the two most intense of these isotropic resonances occur at 334 and 412 ppm, i.e., at the same shift position as those of the main peaks in the ^{23}Na spectra of the NaBi-II (Fig. 4d). This would indicate that the ordering scheme of the interlayer sodiums in the NaBi-H-I material is largely the same as that observed in the NaBi-II, with other local sodium environments generated from possible structural disorder in layer stacking and layer defects.

DISCUSSION

The birnessite spectra show significantly lower shifts than those observed for other mixed valence sodium manganese oxides reported in our previous ^{23}Na NMR studies (Aldi et al. in preparation). In the cited work, sodium manganese oxides containing Mn^{3+} and Mn^{4+}, such as α-$Na_{2/3}MnO_2$ with a 3 to 1 Mn^{3+}:Mn^{4+} composition, produced noticeably larger shifts (1521 and 1637 ppm) compared to compounds containing only Mn^{3+}, such as α-$NaMnO_2$ (725 ppm).

The observed shifts in the birnessite spectrum are roughly half that of the shifts observed in the Mn^{3+} sodium manganese oxide compounds from the previously mentioned study (Aldi et al. in preparation), despite the presence of ~2/3 Mn^{4+} ions in the triclinic birnessite layers, which would be expected to produce larger shifts. Assuming Mn^{3+} orders within the manganate layers into rows as described in the Introduction (Gaillot et al. 2007; Lanson et al. 2002a), the first implication of these spectra is that interlayer sodium is predominantly ordered near these Mn^{3+}-rich rows. Furthermore, these small hyperfine shifts are also consistent with the structural models proposed in previous work. The model proposed by Post et al. (2002) in which sodium sits at the center of the interlayer spacing, will produce a weak Fermi contact shift, as a result of the two long Na-O_{layer} distances, assuming they still produce sufficient orbital overlap for the through bond transfer of spin density (see also Fig. 1c). Earlier structural studies of other inorganic materials, such as sodium metaborate and wyllieite [$Na_2Fe_2Al(PO_4)_3$], indicate that elongated Na-O bond lengths of 2.6–2.8 Å do occur (Brown and Shannon 1973; Marezio et al. 1963; Miletich and Pertlik 1998). There are also considerably fewer Na^+-O-$Mn^{3+/4+}$ contacts than the sodium environments of the model compounds (6 compared to 18) (Aldi et al. in preparation). Thus, the presence of fewer Na^+-O-$Mn^{3+/4+}$ contacts, as well as longer Na-O bonds could explain the significantly smaller hyperfine shifts seen here, over that expected purely from the oxidation state of the manganese ions. The model proposed by Lanson et al. (2002a) also provides a plausible positional scheme in which interlayer sodium forms a distinct bond with an oxide ion of a single MnO_2 layer, clearly allowing a stronger hyperfine shift, but producing only three Na^+-O-$Mn^{3+/4+}$ interactions (see also Fig. 1d). In this case, the mechanism that leads to a smaller observed hyperfine shift in NaBi-H-I and NaBi-II would be dominated by the significantly fewer Na^+-O-$Mn^{3+/4+}$ interactions via a more conventional Na-O bond distance.

The two ^{23}Na resonances found in the NaBi-I are associated with large asymmetry parameters, η, of 0.7 and 1.0 for Sites 1 and 2, respectively, based on our spectral simulations. Large η values indicate highly asymmetric local environments, which is

in support of interlayer sodium shifted off-center and associated with a single manganese oxide layer, i.e., the model of Lanson et al. (2002a). The simulations could not be optimized to capture some weak intensity of the left shoulder of the central transition in the 4.7 T spectrum (see inset of Fig. 3e). This discrepancy could arise from limitations of the simulation software in which infinite spinning is assumed. It is also possible that the intensity not expressed in the simulation represents a minor amount of a third sodium environment around 480–500 ppm. Such an environment is resolved in the 14.1 T spectrum of the NaBi-H-I material at 491 ppm (Fig. 4b) and could therefore also be present in some, much smaller amount in NaBi-II (Fig. 4d).

Ordering schemes of interlayer cations and layer charge distribution that could explain two sodium sites with a ratio of close to 1:1 were examined. A shifted sodium site, as given in the model by Lanson et al. (2002a), was assumed initially, since this simplifies the analysis considerably. Since in this model, sodium is covalently bonded to only one of the two layers, the distribution of layer charge will be a more significant factor determining the local environment of sodium than the registry between the layers. Following from the ordering of Mn^{3+} ions into rows separated by two rows rich in Mn^{4+} ions, two unique sodium environments can be generated by staggering the sodium site along these Mn^{3+} rows, either above or below the layer; one type of ion is coordinated via oxygen to two Mn^{4+} and one Mn^{3+} (Fig. 5a) and the second is coordinated via oxygen to one Mn^{4+} and two Mn^{3+} (Fig. 5b). A third site is also possible (Fig. 5c), but since this is near Mn^{4+} ions only, it is likely to be higher in energy.

The sodium environment coordinated to two Mn^{4+} (Fig. 5a) would give rise to the higher of the two observed isotropic shifts in the ^{23}Na NMR spectra of this sample (Fig. 4d), based on the higher shifts expected for Mn^{4+}-O-Na contacts compared to Mn^{3+}-O-Na ions. With this assignment, the 14.1 T spectrum of the more disordered NaBi-H-I material becomes more informative (Fig. 4b). The two most intense resonances of the high-field NaBi-H-I spectrum at 334 and 412 ppm, are the same as those observed in the ordered NaBi-II material, are separated by about 80 ppm and differ by only one Mn^{3+}, and are therefore assigned to the environments nearby one and two Mn^{4+} ions, respectively. Similarly, a third resonance at 491 ppm is separated by about 80 ppm from the 412 ppm environment. On this basis, the 491 ppm resonance is assigned to a sodium environment coordinated to three Mn^{4+} ions (Fig. 5c), which, although not an ideal environment for charge balance, may occur in birnessites with a certain degree of layer and interlayer cation disorder. Furthermore, this indicates that the Mn^{4+}-rich rows of the more ordered NaBi-II material are almost, if not completely, vacant of interlayer sodium. Finally, the fact that the spectra can be readily explained based on the proximity of Na^+ to one, two, or three Mn^{4+} ions, provides further support for the off-center model: more than three resonances are expected for sodium environments located in the center of the layer since configurations generated by binding to two layer O atoms need to be considered. This results in many more local environments $Na(OMn^{3+}_xOMn^{4+}_{6-x})$ (where we have ignored the binding to the waters in the layers in this formula) in systems that are not fully ordered, or where there is no registry of the ordering between the layers.

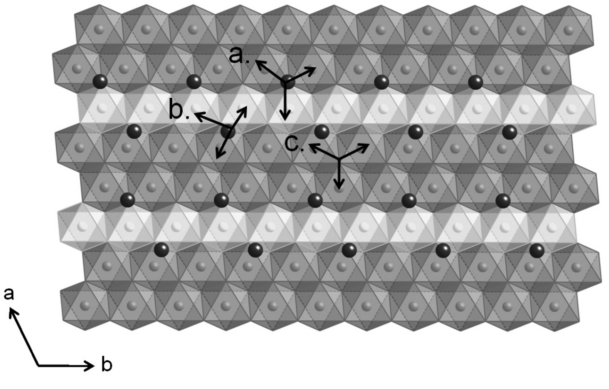

FIGURE 5. Representation of a possible cation ordering scheme for sodium, assuming Mn^{3+}-rich rows (light gray) ordered along **b** separated by two Mn^{4+}-rich rows (dark gray). Interlayer cations (black) are staggered along the ordered rows of Mn^{3+} resulting in two sodium environments on either side of the layer, although all Na^+ are shown on one side in this idealized structure. One sodium site (**a**) is coordinated, via oxygen, to two Mn^{4+} ions and one Mn^{3+} ions. The second sodium site (**b**) is coordinated, via oxygen, to two Mn^{3+} ions and one Mn^{4+}ions. A third, less favorable site (**c**) where Na^+ is coordinated to three Mn^{4+} ions may be possible due to some disorder of interlayer sodium.

The effect of the Jahn-Teller distortions has not been considered in the analysis and assignment of the observed shifts in this study. In the previously mentioned work on sodium manganese oxide model compounds, the presence of Jahn-Teller distortions had a significant impact on shifts (Aldi et al. in preparation). For example, comparison of α- and β-$Na_{2/3}MnO_2$, layered materials in which the slightly lower Mn average oxidation state of the β-form gives rise to a Jahn-Teller distortion, shows α-$Na_{2/3}MnO_2$ to have resonances with notably larger overall shifts (1521 and 1637 ppm) than those observed in spectra of β-$Na_{2/3}MnO_2$ (794 and 1112 ppm) (Aldi et al. in preparation). We considered the different environments generated by the preferential ordering of Na^+ ions with respect to the orientation of the Jahn-Teller distorted Mn^{3+} ions and the possible effects that this might have on the hyperfine shifts. Jahn-Teller distortions may also contribute to the differences in shifts between the three resonances, however we found no simple assignments to specific local environments. Future work will use density functional theory calculations, as was performed in our previous sodium manganese oxide compounds paper (Aldi et al. in preparation), to explore this effect.

ACKNOWLEDGMENTS

This work was supported by the National Science Foundation through Collaborative Research in Chemistry (CHE-0714183). K.A.A. thanks the National Science Foundation for support via the Integrated Graduate Education and Research Training fellowship (Award No. 0549370). K.A.A. thanks Lesley Holmes for data collection of high-field fast MAS data at Keemilise ja Bioloogilise Füüsika Instituut, and Ulla Gro Nielsen for helpful discussions. J.C. is indebted to the Generalitat de Catalunya for providing funding through a Beatriu de Pinós postdoctoral fellowship.

REFERENCES CITED

Bargar, J.R., Fuller, C.C., Marcus, M.A., Brearley, A.J., De la Rosa, M.P., Webb, S.M., and Caldwell, W.A. (2009) Structural characterization of terrestrial microbial Mn oxides from Pinal Creek, Arizona. Geochimica et Cosmochimica Acta, 73, 889–910.

Brown, I.D. and Shannon, R.D. (1973) Empirical bond-strength-bond-length curves for oxides. Acta Crystallographica, A29, 266–282.

Carlier, D., Menetrier, M., Grey, C.P., Delmas, C., and Ceder, G. (2003) Understanding the NMR shifts in paramagnetic transition metal oxides using density

functional theory calculations. Physical Review B, 67, 174103.
Carlier, D., Blangero, M., Menetrier, M., Pollet, M., Doumerc, J.P., and Delmas, C. (2009) Sodium Ion Mobility in Na_xCoO_2 ($0.6<x<0.75$) Cobaltites studied by ^{23}Na MAS NMR. Inorganic Chemistry, 48, 7018–7052.
Cheetham, A.K., Dobson, C.M., Grey, C.P., and Jakeman, R.J.B. (1987) Paramagnetic shift probes in high-resolution solid-state NMR. Nature, 328, 706–707.
Drits, V.A., Silvester, E., Gorshkov, A.I., and Manceau, A. (1997) Structure of synthetic monoclinic Na-rich birnessite and hexagonal birnessite. 1. Results from X-ray diffraction and selected-area electron diffraction. American Mineralogist, 82, 946–961.
Drits, V.A., Lanson, B., and Gaillot, A.C. (2007) Birnessite polytype systematics and identification by powder X-ray diffraction. American Mineralogist, 92, 771–788.
Feng, Q., Sun, E.H., Yanagisawa, K., and Yamasaki, N. (1997) Synthesis of birnessite-type sodium manganese oxides by solution reaction and hydrothermal methods. Journal of the Ceramic Society of Japan, 105, 564–568.
Feng, Q., Lui, L., and Yanagisawa, K. (2000) Effects of synthesis parameters on the formation of birnessite-type manganese-oxides. Journal of Materials Science Letters, 19, 1567–1570.
Fuller, C.C. and Harvey, J.W. (2000) Reactive uptake of trace metals in the hyporheic zone of a mining-contaminated stream, Pinal Creek, Arizona. Environmental Science and Technology, 34, 1150–1155.
Gaillot, A.C., Drits, V.A., Manceau, A., and Lanson, B. (2007) Structure of the synthetic K-rich phyllomanganate birnessite obtained by high-temperature decomposition of $KMnO_4$—Substructures of K-rich birnessite from 1000 °C experiment. Microporous and Mesoporous Materials, 98, 267–282.
Giovanoli, R., Stahli, E., and Feitknecht, W. (1970) Uber Oxidhydroxide des vierwertigen Mangans mit Schichtengitter. Helvetica Chimica Acta, 53, 209–220.
Glasby, G.P., Ed. (1977) Marine manganese deposits. Elsevier Oceanography Series, 15, 523. Elsevier, Amsterdam.
Golden, D.C., Dixon, J.B., and Chen, C.C. (1986) Ion-Exchange, thermal transformations, and oxidizing properties of birnessite. Clays and Clay Minerals, 34, 511–520.
Grey, C.P. and Dupré, N. (2004) NMR studies of cathode materials for lithium-ion rechargeable batteries. Chemical Reviews, 104, 4493–4512.
Harvey, J.W. and Fuller, C.C. (1998) Effect of enhanced manganese oxidation in the hyporheic zone on basin-scale geochemical mass balance. Water Resources Research, 34, 623–636.
Johnson, E.A. and Post, J.E. (2006) Water in the interlayer region of birnessite: Importance in cation exchange and structural stability. American Mineralogist, 91, 609–618.
Kim, J., Middlemiss, D.S., Chernova, N.A., Zhu, B.Y.X., Masquelier, C., and Grey, C.P. (2010) Linking local environments and hyperfine shifts: A combined experimental and theoretical (31)P and (7)Li solid-state NMR study of paramagnetic Fe(III) phosphates. Journal of the American Chemical Society, 132, 16825–16840.
Kuma, K., Usui, A., Paplawsky, W., Gedulin, B., and Arrhenius, G. (1994) Crystal-structures of synthetic 7 Å and 10 Å manganates substituted by monovalent and divalent-cations. Mineralogical Magazine, 58, 425–447.
Lanson, B., Drits, V.A., Silvester, E., and Manceau, A. (2000) Structure of H-exchanged hexagonal birnessite and its mechanism of formation from Na-rich monoclinic buserite at low pH. American Mineralogist, 85, 826–838.
Lanson, B., Drits, V.A., Feng, Q., and Manceau, A. (2002a) Structure of synthetic Na-birnessite: Evidence for a triclinic one-layer unit-cell. American Mineralogist, 87, 1662–1671.
Lanson, B., Drits, V.A., Gaillot, A.C., Silvester, E., Plancon, A., and Manceau, A. (2002b) Structure of heavy-metal sorbed birnessite: Part 1. Results from X-ray diffraction. American Mineralogist, 87, 1631–1645.
Liu, L., Feng, Q., and Yanagisawa, K. (2000) Characterization of birnessite-type sodium manganese oxides prepared by hydrothermal reaction process. Journal of Materials Science Letters, 19, 2047–2050.
Lopano, C.L., Heaney, P.J., Post, J.E., Hanson, J., and Komarneni, S. (2007) Time-resolved structural analysis of K- and Ba-exchange reactions with synthetic Na-birnessite using synchrotron X-ray diffraction. American Mineralogist, 92, 380–387.
Mackenzie, K.J.D. and Smith, M.E. (2002) Multinuclear Solid-state NMR of Inorganic Materials, 727 p. Elsevier, Amsterdam.
Manceau, A., Lanson, B., and Drits, V.A. (2002) Structure of heavy metal sorbed birnessite. Part III: Results from powder and polarized extended X-ray absorption fine structure spectroscopy. Geochimica et Cosmochimica Acta, 66, 2639–2663.
Marezio, M., Plettinger, H.A., and Zachariasen, W.H. (1963) The bond lengths in the sodium metaborate structure. Acta Crystallographica, 16, 594–595.
McKenzie, R.M. (1967) Sorption of cobalt by manganese minerals in soils. Australian Journal of Soil Research, 5, 235-246.
McKenzie, R.M. (1980) Adsorption of lead and other heavy-metals on oxides of manganese and iron. Australian Journal of Soil Research, 18, 61–73.
Miletich, R. and Pertlik, F. (1998) Crystal structure of $NaGaTe_2O_6$: Aspects of Te_nO_m polyhedral polymerization in a layer tellurite. Journal of Alloys and Compounds, 268, 107–111.
O'Reilly, S.E. and Hochella, M.F. (2003) Lead sorption efficiencies of natural and synthetic Mn and Fe-oxides. Geochimica et Cosmochimica Acta, 67, 4471–4487.
Pena, J., Kwon, K.D., Refson, K., Bargar, J.R., and Sposito, G. (2010) Mechanisms of nickel sorption by a bacteriogenic birnessite. Geochimica et Cosmochimica Acta, 74, 3076–3089.
Post, J.E. (1999) Manganese oxide minerals: Crystal structures and economic and environmental significance. Proceedings of the National Academy of Sciences, 96, 3447–3454.
Post, J.E. and Veblen, D.R. (1990) Crystal-structure determinations of synthetic sodium, magnesium, and potassium birnessite using TEM and the Rietveld method. American Mineralogist, 75, 477–489.
Post, J.E., Heaney, P.J., and Hanson, J. (2002) Rietveld refinement of a triclinic structure for synthetic Na-birnessite using synchrotron powder diffraction data. Powder Diffraction, 17, 218–221.
Potter, R.M. and Rossman, G.R. (1979) Tetravalent manganese oxides; identification, hydration, and structural relationships by infrared-spectroscopy. American Mineralogist, 64, 1199–1218.
Rogers, D.B., Germann, R.W., and Arnott, R.J. (1965) Effect of trivalent manganese on the crystal chemistry of some lithium spinels. Journal of Applied Physics, 36, 2338–2343.
Sherman, D.M. and Peacock, C.L. (2010) Surface complexation of Cu on birnessite (δ-MnO_2): Controls on Cu in the deep ocean. Geochimica et Cosmochimica Acta, 74, 6721–6730.
Silvester, E., Manceau, A., and Drits, V.A. (1997) Structure of synthetic monoclinic Na-rich birnessite and hexagonal birnessite. 2. Results from chemical studies and EXAFS spectroscopy. American Mineralogist, 82, 962–978.
Toner, B., Manceau, A., Webb, S.M., and Sposito, G. (2006) Zinc sorption to biogenic hexagonal-birnessite particles within a hydrated bacterial biofilm. Geochimica et Cosmochimica Acta, 70, 27–43.
Villalobos, M., Toner, B., Bargar, J., and Sposito, G. (2003) Characterization of the manganese oxide produced by Pseudomonas putida strain MnB1. Geochimica et Cosmochimica Acta, 67, 2649–2662.
Villalobos, M., Lanson, B., Manceau, A., Toner, B., and Sposito, G. (2006) Structural model for the biogenic Mn oxide produced by *Pseudomonas putida*. American Mineralogist, 91, 489–502.
Webb, S.M., Tebo, B.M., and Bargar, J.R. (2005) Structural characterization of biogenic Mn oxides produced in seawater by the marine *bacillus sp.* strain SG-1. American Mineralogist, 90, 1342–1357.

Manuscript received July 1, 2011
Manuscript accepted January 16, 2012
Manuscript handled by M. Darby Dyar